

CONSTRAINING THE BARYON FRACTION IN THE WARM HOT INTERGALACTIC MEDIUM AT LOW REDSHIFTS WITH PLANCK DATA

R. GÉNOVA-SANTOS^{1,2}, F. ATRIO-BARANDELA³, F.-S. KITaura⁴, J. P. MÜCKET⁴*Draft version May 19, 2015*

ABSTRACT

We cross-correlate foreground cleaned Planck Nominal Cosmic Microwave Background (CMB) maps with two templates constructed from the Two-Micron All-Sky Redshift Survey of galaxies. The first template traces the large-scale filamentary distribution characteristic of the Warm-Hot Intergalactic Medium (WHIM) out to $\sim 90h^{-1}\text{Mpc}$. The second traces preferentially the virialized gas in unresolved halos around galaxies. We find a marginal signal from the correlation of Planck data and the WHIM template with a signal-to-noise from 0.84 to 1.39 at the different Planck frequencies, and with a frequency dependence compatible with the thermal Sunyaev-Zel'dovich (tSZ) effect. When we restrict our analysis to the 60% of the sky outside the plane of the Galaxy and known point sources and galaxy clusters, the cross-correlation at zero lag is $0.064 \pm 0.051\mu\text{K}$. The correlation extends out to $\approx 6^\circ$, which at the median depth of our template corresponds to a physical length of $\sim 6 - 8 h^{-1}\text{Mpc}$. On the same fraction of the sky, the cross-correlation of the CMB data with the second template is $< 0.17 \mu\text{K}$ (95% C.L.), providing no statistically significant evidence of a contribution from bound gas to the previous result. This limit translates into a physical constraint on the properties of the shock-heated WHIM of a log-normal model describing the weakly nonlinear density field. We find that our upper limit is compatible with a fraction of 45% of all baryons residing in filaments at overdensities $\sim 1 - 100$ and with temperatures in the range $10^{4.5} - 10^{7.5}\text{K}$, in agreement with the detection at redshift $z \sim 0.5$ of Van Waerbeke et al. (2014).

Subject headings: Cosmic Background Radiation. Cosmology: theory. Cosmology: observations

1. INTRODUCTION

The cosmological evolution of baryons within dark matter halos is still an open problem. While at redshifts $z \sim 2$ the baryon fraction residing in collapsed structures is close to the cosmic mean (Rauch et al. 1997; Weinberg et al. 1997), at redshifts $z \sim 0$ is $\sim 40 - 50\%$ smaller than the measured value (Fukugita & Peebles 2004; Shull et al. 2012). Early hydrodynamical simulations suggested that the unidentified baryons could reside in mildly-nonlinear filamentary structures with temperatures $0.01 - 1 \text{ keV}$ and overdensities $\delta_B < 10^3$ the mean baryonic density, known as Warm-Hot Intergalactic Medium (WHIM) (Cen & Ostriker 1999; Dave et al. 2001). Understanding the distribution of baryons and dark matter from galaxies to clusters is essential to explain the formation and evolution of structure in the Universe. Consequently, a great observational effort is being devoted to detect the WHIM signature, mostly by searching for absorption lines due to highly ionized heavy elements. Some detections have been reported in the far-ultraviolet (Tripp et al. 2008) and in the soft X-ray (Nicastro et al. 2005; Buote et al. 2009) bands but these detections are ambiguous or controversial. In some cases they could not be confirmed by later studies (Yao et al. 2012). In others it has not yet been settled whether the detected lines arise from the WHIM or from individual

galaxies or groups within the filaments (Williams et al. 2013). Attempts have also been made to detect signatures of the WHIM diffuse X-ray emission; Werner et al. (2008) reported a detection from a filament connecting two clusters, with properties compatible with the WHIM.

The baryons in this WHIM plasma do not only contribute to the diffuse X-ray background but they also produce CMB distortions by means of the thermal Sunyaev-Zeldovich (tSZ) effect (Sunyaev & Zel'dovich 1970). This effect could probe the physical state of baryons in the WHIM phase better than X-rays thanks to its milder dependence on the gas density. An alternative to finding a direct evidence towards superclusters of galaxies (Molnar & Birkinshaw 1998; Génova-Santos et al. 2005) is to correlate CMB maps with galaxy templates tracing large scale structures. This approach was first used by Hernández-Monteagudo et al. (2004), whose measured signal was dominated by clusters of galaxies. A similar analysis was carried out by Suarez-Velásquez et al. (2013a) and, again, the correlation was most-likely due to foreground residuals and to random alignments between structure in the data and the matter template, and not to WHIM. In Atrio-Barandela & Mücke (2006) and Atrio-Barandela et al. (2008) we computed the power spectra of the thermal and kinetic SZ anisotropies due to the WHIM, calculations that were later refined by Suarez-Velásquez, Mücke & Atrio-Barandela (2013b). We used these models in Génova-Santos et al. (2009, 2013) to fit these SZ spectra to CMB data through a Monte-Carlo Markov Chain analysis. Although adding the SZ from the WHIM to the ΛCDM CMB power spectrum improved the quality of the fit, this improvement was not statistically significant and it did not favor the

¹ Instituto de Astrofísica de Canarias, 38200 La Laguna, Tenerife, Spain; rgs@iac.es

² Departamento de Astrofísica, Universidad de La Laguna (ULL), 38206 La Laguna, Tenerife, Spain

³ Física Teórica, Universidad de Salamanca, 37008 Salamanca, Spain; atrio@usal.es

⁴ Leibniz Institut für Astrophysik, 14482 Potsdam, Germany; kitaura,jpmuecket@aip.de

inclusion of a new component in the model.

While these earlier attempts based on WMAP data only provided upper limits to the WHIM contribution, the tSZ effect has been shown to be effective at detecting baryonic filaments in the denser and hotter medium of interacting cluster pairs (Planck Collaboration 2013a). This study was greatly benefited from the finer angular resolution and wider frequency coverage of *Planck* data, which helped to isolate better the tSZ signal from other components. Recently, Van Waerbeke et al. (2014) reported a positive correlation between mass maps reconstructed from the Canada France Hawaii Telescope Lensing Survey and a tSZ map constructed from Planck data with an overall significance of 6σ and extending out to linear scales of ~ 10 Mpc. They interpreted this correlation as arising from WHIM at $z \sim 0.4$ and with temperatures in the range $10^5 - 10^6$ K, depending on the gas bias and the electron density on the filaments. However, the measured signal could also come from gas within virialized halos, especially after the Planck Collaboration (2013b) showed that the tSZ anisotropy exists down to masses as low as $\sim 2 \times 10^{11} M_\odot$. Ursino et al. (2014) suggested to cross-correlate X-ray and SZ maps to trace the WHIM distribution and found that the small-scale correlation would be dominated by the high-redshift WHIM, that again would probe the WHIM at early times.

The Van Waerbeke et al. (2014) detection could indicate that a large fraction of the “missing” baryons reside in a low-density warm plasma that traces the dark matter distribution. Equally important to this high redshift observation is to probe the state of the WHIM gas at lower redshifts. If filaments reside in the large-scale dark matter potential wells, then tracers of dark matter distribution at low redshifts will correlate with the WHIM signal both in X-ray and radio, irrespectively of the redshift. If the gas is confined to low mass halos then its tSZ will correlate with the distribution of galaxies. In this article we compute the cross-correlation of the temperature fluctuations of the CMB with two templates: (A) the projected matter density reconstructed from the distribution of galaxies within $\leq 150h^{-1}\text{Mpc}$ from the Local Group (Kitaura 2012a) to investigate the properties of the WHIM at redshifts $z < 0.05$ and (B) the density of the same galaxies projected along the line of sight to study the contribution of virialized gas in halos below the mass threshold of the matter template. The outline of the paper is as follows: In Section 2 we describe our data sets; we describe our procedure for reducing the foreground contribution of Planck Nominal maps corresponding to the March 2013 release (Planck Collaboration et al. 2014a) and the construction of the galaxy and the dark matter templates. In Section 3 we explain the filtering and the masking that we apply to our data. In Section 4 we present the results of the correlation between the templates and the CMB data; in Section 5 we discuss the implications on the WHIM physical models and, finally, in Section 6 we summarize our main conclusions.

2. THE DATA

2.1. *Planck* foreground cleaned maps

As a tracer of the tSZ signal we use Planck DR1 maps (Planck Collaboration et al. 2014a), which cover a wide

frequency range delimited by nine independent channels, provided by the LFI (30, 44 and 70 GHz) and the HFI (100, 143, 217, 353, 545 and 857 GHz) instruments. Apart from the cosmological signal, and the potential tSZ signature, these maps contain significant foreground contamination, mainly synchrotron and free-free emissions at low frequency and thermal dust at high frequency, as well as CO emission and zodiacal light. We carefully clean all these contributions to obtain foreground cleaned maps at each frequency that will be a combination of three components: CMB, tSZ and instrumental noise. At the HFI frequencies, where the zodiacal light is more important, we use publicly-available maps where this contaminant has been removed, as described in Planck Collaboration et al. (2014b). All these maps are produced using HealPix⁵ (Gorski et al. 2005) pixelization, with resolution of $N_{\text{side}} = 1024$ and 2048 for the LFI and HFI instruments, respectively. All Planck-related products used in this paper have been downloaded from the Planck Legacy Archive⁶.

To perform the correction of the thermal dust emission we use the maps from the Planck dust model that, in each sky pixel with HealPix resolution $N_{\text{side}} = 2048$, contain the three parameters that define the modified black-body (MBB) emission law (dust-grains temperature, emissivity index and optical depth) at the reference frequency of 353 GHz. These maps have been obtained on a pixel-by-pixel basis by a χ^2 -minimization fit of the model to the HFI and IRAS data, as explained in Planck Collaboration et al. (2014c). In order to accurately estimate the contribution of this emission at each Planck frequency we evaluate the spectral model in each pixel and convolve it with the passband of each detector. We apply this color correction using the publicly-available routine `hfi_colour_correction`. Similarly, to clean the synchrotron and free-free emissions we use maps, delivered by the Planck Collaboration, that at each pixel contain the amplitude of the signal at the reference frequency of 30 GHz and a spectral index obtained by fitting a power-law model to the Planck lowest frequencies (Planck explanatory supplement 2013). In this case a color correction using the same routine mentioned above, is also applied to estimate the flux weighted in each band. The maps of the low-frequency and high-frequency foregrounds are subtracted from each frequency map.

The last step of the process is to clean the CO emission, which is especially important in the 100, 217 and 353 GHz channels as a result of the (1-0), (2-1) and (3-2) rotational transition lines, respectively. As explained in the Planck explanatory supplement (2013) and in Planck Collaboration et al. (2014e), the Planck Consortium has delivered three different types of CO correction maps. The type 2 maps have the highest signal to noise, at the expense of having possible residuals from other foregrounds, but they are available only for 100 and 217 GHz. Type 1 maps are available for the three frequencies, but have a much lower signal-to-noise and we found them not to be useful for cleaning the data. Then, we do not apply any correction to 353 GHz and we clean

⁵ <http://healpix.jpl.nasa.gov/>

⁶ <http://www.sciops.esa.int/index.php?project=planck&page=PlanckLegacyArchive>

the 100 and 217 GHz maps using the type 2 maps, a procedure that noticeably reduces the CO contamination at these frequencies.

Our final foreground cleaned maps are shown in Figure 1, for frequencies 44 to 353 GHz. The foreground contamination in these maps has been clearly reduced. Although there are some residuals of Galactic emission along the plane, the signal in the rest of the sky is dominated by the CMB fluctuations. The power spectra of these maps nicely match the theoretical spectrum of the concordance model with the cosmological parameters measured by Planck. The foreground cleaning procedure has operated best at 353 GHz since is at this frequency where the Planck dust model was evaluated. The cleaning at other frequencies is affected by possible errors in the MBB model or in the determination of the emissivity index. The residual dust contamination in the Galactic plane diminishes at lower frequencies. At 44 and 70 GHz some residual from synchrotron and free-free emission are visible along the plane. Although not shown here, the 30 GHz map was also used in our analysis. On the contrary, we ignored the 545 and the 857 GHz due to having stronger foreground residuals.

In order to avoid sky regions affected by emission of diffuse foregrounds, point sources or galaxy clusters, we apply different masks. We first apply the Planck mask derived from the Commander-Ruler component separation method⁷ (Planck Collaboration et al. 2014d), which retains 82% of the sky. Most of the masked pixels are associated with point sources; a stripe along the Galactic plane of $\sim 10^\circ$ width in Galactic latitude is also removed, accounting for about 8% of the sky. This Galactic mask is sufficient to remove the residual Galactic emission that appear in the maps of Figure 1. To avoid regions affected by potentially fainter residuals we apply more conservative masks. We perform the analysis using three different Planck Galactic masks⁸. The total sky fractions retained in the three resulting masks are respectively 73.3, 55.8 and 37.1%, but we follow the practice to refer to these masks as the 70%, 60% and 40% masks. Finally, we need to eliminate possible tSZ signals from Galaxy clusters. Although the Commander-Ruler mask already removes some clusters, to be conservative we also mask all pixels within a radius of 0.5° around all known clusters with redshifts $z \leq 0.04$ and with X-ray luminosities $L_X \geq 10^{43} \text{erg/s}$ in the ROSAT [0.1-2.4]KeV band. The cross-correlation functions are computed on maps with a resolution $N_{\text{side}} = 128$. All masks are downgraded to this pixel resolution and, conservatively, we only retain pixels with values greater than 0.75.

2.2. Density field templates

We will analyze two possible distributions of the missing baryon fraction: (A) unbound gas following the filamentary structure of the large scale matter distribution, and (B) virialized gas in unresolved halos traced by the spatial distribution of galaxies. Hereafter, we will refer to the two templates tracing these distributions as the matter template M and the galaxy template M_g , respectively. The reconstruction technique of the matter den-

sity field is based on a Bayesian Networks Machine Learning algorithm (the Kigen-code) which self-consistently samples the initial density fluctuations compatible with the observed galaxy distribution and a structure formation model given by second order Lagrangian perturbation theory (Kitaura 2012a; Kitaura et al. 2012b). As a tracer of the matter density field we used the Two-Micron All-Sky Redshift Survey (2MRS, Huchra et al. 2012). The method recovers the non-linear structures like knots, sheets, filaments and voids in the cosmic web to great accuracy. The reconstruction is performed on a cubic box since it requires to compute FFTs. In previous works we reconstructed the density field using boxes of side $160h^{-1}\text{Mpc}$ (Kitaura et al. 2012b) and $180h^{-1}\text{Mpc}$ (Heß et al. 2013) and found compatible results, proving that the boundary effects are unimportant. In this work, the reconstructed density field on the sphere includes modes with wavelengths up to $110 - 130h^{-1}\text{Mpc}$. For our theoretical estimates we take the average depth of the reconstructed density field to be $90h^{-1}\text{Mpc}$. The template built through this reconstruction technique is produced using a HealPix resolution $N_{\text{side}} = 128$. The matter distribution shows well defined filaments, characteristic of the mildly non-linear regime that we assume to be a good tracer of the WHIM. As the reconstruction also traces the galaxy distribution, it is sensitive to the hot halos surrounding galaxies that have been recently detected (Anderson & Bregman 2011; Dai et al. 2012).

Low-mass galaxy clusters or galaxy groups below the threshold mass of our previous template could also produce a detectable tSZ anisotropy (Planck Collaboration 2013b). The pixels at $N_{\text{side}} = 128$ have an angular size of $\sim 0.5^\circ \times 0.5^\circ$ and if the virialized and unbound gas were to follow the same spatial distribution we would not have enough angular resolution to disentangle a potential signal associated to collapsed low-mass systems from the signal of the unbound WHIM gas. Most likely the virialized gas detected by *Planck* is better traced by the galaxies themselves. Under this assumption, we can check the amplitude of this contribution using a template of the projected density of galaxies. To make the comparison more meaningful, we project along the line of sight the same sample of 2MRS galaxies that went into the reconstruction of the matter density field described above. By construction, this galaxy template traces the hot circumgalactic halo. At $10h^{-1}\text{Mpc}$ a pixel of half degree side corresponds to $80h^{-1}\text{Kpc}$, slightly larger than the halo but at $60h^{-1}\text{Mpc}$, the average depth of our template, it corresponds to $\sim 500h^{-1}\text{Kpc}$, much larger than the virial radius of the detected halos (Anderson & Bregman 2011). Therefore, this template could potentially also trace the gas outside the circumgalactic halo.

3. DATA PROCESSING

The tSZ signal due to WHIM has an amplitude of about few μK but the expected cross-correlation with a matter template out to $\sim 90 - 120h^{-1}\text{Mpc}$ is expected to be $\sim 0.03 - 0.3 \mu\text{K}$ (Suarez-Velázquez et al. 2013a). At any frequency ν , the error bar on the cross-correlation of the CMB data $T(\nu)$ with a matter template M , $\langle T(\nu)M \rangle(\theta)$, is dominated by the intrinsic CMB anisotropy. In order to obtain a statistically significant detection, the data needs to be processed further. There

⁷ Mask named COM_CompMap_Mask-rulerminimal_2048_R1.00.fits in the Planck Legacy Archive.

⁸ To be found in the HFI_Mask_GalPlane_2048_R1.10.fits file.

are two possibilities: (1) use the 217 GHz channel, the frequency of the tSZ null, to subtract off the intrinsic CMB signal while preserving the tSZ anisotropy and (2) construct a Compton parameter y -map combining all frequencies to remove all components from the data except the tSZ, as it was done in Planck Collaboration et al. (2014g). Subtracting the 217 GHz channel from the other maps will increase the noise and add the 217 GHz foreground residuals to those remaining at other frequencies but, when constructing a y -map the frequency information of the tSZ effect will be lost. This information could be crucial to distinguish correlations due to random alignments or stripes present in the data from the true effect due to the WHIM. Therefore, in this article we will use method (1), i.e. we will subtract the correlation function at 217 GHz from those at other frequencies.

In Figure 2 we plot the power spectra of the subtracted maps. We only analyzed maps with HealPix resolution $N_{\text{side}} = 128$. Effectively, all the maps have been downgraded to the same resolution by the pixel window, which dominates over that of the beam. When subtracting the 217 GHz from the maps at other frequencies, we are effectively removing the intrinsic CMB signal. At multipoles $\ell \leq 20$, the power spectra scale as $C_\ell \sim \ell^{-2}$, compatible with being dominated by marginal CMB residuals, instrumental ($1/f$) noise and foreground residuals, while at $\ell \geq 60$ the spectra are compatible with white noise. Maps could be correlated even if there is not any WHIM signal present. To reduce these spurious correlations, maps can be filtered by removing the lowest multipoles up to any given ℓ_{cut} . Since at $N_{\text{side}} = 128$ the highest multipole is $\ell_{\text{max}} \sim 256$, removing modes up to $\ell_{\text{cut}} = 60$ could erase a significant part of the WHIM signal. As a compromise, we set $\ell_{\text{cut}} = 20$. Finally, to reduce the transfer of power from galactic residuals to multipoles at all scales, before computing the multipole expansion of the original map, 20% of the sky around the galactic plane is masked.

In Figure 3 we show the 353-217 GHz difference CMB map (top row), the matter template (middle) and the galaxy template (bottom) before and after the lowest multipoles have been removed. If initially the CMB data is dominated by noise and foreground residuals, cutting the lowest multipole reduces both contributions. Stripes due to *Planck* scanning strategy are still present and, with the smaller noise levels, they are more clearly seen in the filtered map. Filtering introduces aliasing between different multipoles, giving rise to significant temperature anisotropies next to the galactic plane; in addition, fringing is also present. Nevertheless, these artifacts do not pose a serious problem. In fact, we can compute the CMB-template cross-correlation with different masks, removing from 20% to 60% of the sky, to test the effect of these systematics.

For consistency we also remove the lowest multipoles of the templates. The matter template is shown in the middle row of Figure 3 before (left panel) and after (right panel) filtering. Since the template has little power at large scales (see Figure 2 of Suarez-Velázquez 2013a), the filtered template has very similar structure to the original template and the filaments show a very similar distribution. The template of the projected density of galaxies before (left) and after (right) filtering is shown in the bottom row of Figure 3. This template has a sim-

ilar large structure as the matter distribution but is less smooth at small scales as one could expect of the spatial distribution of clustered halos. Again, notice that filtering the lowest multipoles does not affect the overall distribution of galaxies.

A visual comparison of the filtered templates of matter (right middle panel of Figure 3) and projected density of galaxies (right bottom panel) shows that they have a very similar large scale structure, as one could expect since the galaxy template contains all galaxies that were used to reconstruct the matter distribution. Their main difference is at small scales where the matter template is a smoother function. Then, one can assume that the matter template would trace better the unbound WHIM gas residing in the large scale dark matter potential wells while the galaxy template would trace the circumgalactic gas in virialized halos. However, as discussed in Sec. 2.2, both templates could trace both gas components, probably with different relative weights, since the matter template includes the contribution from the hot halos around galaxies and for most galaxies the angular scale subtended by the virial radius of those circumgalactic halos is smaller than the pixel size at Healpix $N_{\text{side}} = 128$ resolution.

To summarize, our pipeline performs the following steps on the foreground cleaned Planck Nominal maps: first, the galactic plane, point sources and clusters are masked out. Second, CMB data and templates are transformed to spherical harmonic space and all multipoles with $\ell < 20$ are removed. Next, all maps are downgraded to a HealPix resolution of $N_{\text{side}} = 128$, the resolution of the matter template. Templates are normalized to zero mean and unit variance so the cross-correlation is given in temperature units. Finally, the cross-correlations $C_\nu = \langle T_\nu * M \rangle$ are calculated at each frequency ν using three different masks that preserve 70, 60 and 40 per cent of the sky.

4. RESULTS

In order to remove the contamination from the primordial CMB, we subtract the 217 GHz correlation function from those calculated at all other frequencies. If the cross-correlation $(C_\nu - C_{217})$ is dominated by the tSZ effect due to the WHIM traced by the template, then it must scale as $(C_\nu - C_{217}) \sim G(\nu)$, reflecting the frequency dependence of the tSZ effect $G(\nu)$. In this case, the reduced cross-correlation $\langle TM \rangle = (C_\nu - C_{217})/G(\nu)$ between a template and the CMB data must be independent of frequency and proportional to the cross-correlation of the template with the Comptonization parameter Y_c , i.e., $\langle TM \rangle \propto \langle Y_c M \rangle$. This reduced correlation function is given in Figure 4; the top row corresponds to the correlation with the matter template (Figure 3 middle right) and the projected galaxy density template (Figure 3 bottom right). Panels (a), (d) correspond to the correlation with LFI frequency maps and (b), (e) to the correlation with HFI frequency maps computed on 60% of the sky; (c) and (f) is the combination of all frequencies for different fractions of the sky. The tSZ is negative in the Raleigh-Jeans part of the spectrum and is positive in the Wien region. The frequency dependence of the tSZ effect varies from $G(30 \text{ GHz}) \simeq -2$ to $G(143 \text{ GHz}) \simeq -1$ and $G(353 \text{ GHz}) \simeq 2.2$. Then, if the cross-correlation of the templates and Planck foreground

cleaned data corresponds to a tSZ contribution, it must be negative for the frequencies below 217 GHz and positive above it. This is what it actually happens. Panels (a), (b), (d) and (e) of Figure 4 show that all correlations have the same sign once divided by $G(\nu)$, indicating that they are consistent with being due to tSZ contribution since their amplitude is similar in all channels and have the correct sign and, although none of our measurements is statistically significant, the correlations with the matter template in the top row are a factor three larger than those with the projected galaxy density in the bottom row. At the origin, the signal-to-noise ratio (SNR) is of order unity, being somewhat larger at angular scales $\theta \sim 2 - 5^\circ$.

In Figure 4 error bars were computed from the rms dispersion of the correlation of 100 random rotated templates with the CMB maps. To explore the sky homogeneously, we select a random set of N_{sim} pixels drawn from a random distribution of all the pixels in the map and compute their angular coordinates (l, b) . Then, we compute the Euler angles that align the north galactic pole with the direction (l, b) of the randomly chosen N_{sim} pixels and rotate the template. Since our template reconstructs the full sky, the area on which the correlation is computed is always defined by the mask, and therefore is the same in all the rotations. By using the same data to compute the correlation and its error bars we include all contributions due to foreground residuals and $1/f$ instrumental noise.

In panels (c) and (f) of Figure 4, we plot the correlation functions after combining the six LFI+HFI channels. For comparison, we plot the results for the three masks used in our study. To combine different frequencies, for each angle we make a weighted average of the correlation functions for different frequencies:

$$\langle TM \rangle_{\text{av}}(\theta) = \frac{\sum_i \langle TM \rangle(\theta, \nu_i) w(\theta, \nu_i)}{\sum_i w(\theta, \nu_i)}, \quad (1)$$

where the sum runs over all the frequencies considered, and $w(\theta, \nu_i) = 1/\sigma(\theta, \nu_i)^2$, with $\sigma(\theta, \nu_i)$ the rms dispersion calculated at position θ in all the rotations of map ν_i . We calculate the error bar associated to this estimator by accounting for possible correlations between frequencies:

$$\sigma(\langle TM \rangle_{\text{av}}(\theta)) = \frac{1}{\sqrt{\sum_i \sum_j w(\theta, \nu_i) \langle TM \rangle_{ij}(\theta) w(\theta, \nu_j)}}, \quad (2)$$

where $\langle TM \rangle_{ij}(\theta) = \langle \langle TM \rangle(\theta, \nu_i) \langle TM \rangle(\theta, \nu_j) \rangle$ represents the covariance between frequencies ν_i and ν_j at position θ . We found that the results for difference frequencies are strongly correlated and for this reason the statistical significance does not improve much by averaging different frequencies. In particular, at zero lag and for the 60% mask, where the covariance is typically between 0.75 and 0.85, we obtain a SNR = 1.26, while the signals for individual frequencies have SNR between 0.84 and 1.39. Our overall statistical significance is never larger than $\text{SNR} \simeq 2$. After averaging over all frequencies, the correlation with the matter template, measured on 60% of the sky, was $\langle TM \rangle(0) = 0.064 \pm 0.051 \mu\text{K}$. Taking this result as an upper limit we obtain $\langle TM \rangle(0) < 0.11 \mu\text{K}$ at 68% C.L. and $< 0.17 \mu\text{K}$ at 95% C.L. Even if the result is not statistically significant, we find that the cross-correlation

is zero at $\theta \sim 6 - 8$ degrees. The average depth of our template is $\sim 60 h^{-1} \text{Mpc}$. At this depth, the zero crossing of the correlation function corresponds to a linear scale of $\sim 6 - 8 h^{-1} \text{Mpc}$. This would be the averaged projected linear size of the WHIM filaments traced by our matter template. This size is reassuringly consistent with the scale found by Van Waerbeke et al. (2014) and could indicate that the effect is real but our template is not deep enough to produce a significant detection.

Comparison of the cross-correlation using different galactic masks allow us to test the effect of fringing and power leakage of the galactic foregrounds into the galactic poles due to our filtering scheme. The oscillation pattern at large distances of the correlation functions shown in Figure 4 is partly produced by this residual fringing. In addition, the number of pairs varies with a scale of $\sim 6^\circ - 10^\circ$, the mean separation between filaments and also the typical angular size of filaments, increasing and decreasing the sample variance component of the error bar accordingly. Notice that when we restrict the analysis to the cleanest regions of the sky, located around the Galactic Poles, the statistical significance of our results increases because even if the error bars are larger due to a bigger sampling variance the signal increases even more.

If the galaxy template traces preferentially the gas stored in halos, it can be used to constrain the contribution due to the halos below the mass threshold of the galaxy clusters excised from our analysis. The cross-correlation between the galaxy density template and the foreground cleaned maps at zero lag in 60% of the sky is also compatible with zero: $\langle TM_g \rangle(0) = 0.022 \pm 0.028 \mu\text{K}$. We obtain an upper limit of $\langle TM_g \rangle(0) < 0.078 \mu\text{K}$ at the 95% confidence level. As we have argued, the matter and the galaxy template trace both the bound and unbound gas components, probably weighing differently each contribution. Comparing with the previous result, the galaxy template provides a more restrictive upper limit that could reflect that the template does not trace the WHIM fully.

5. CONSTRAINTS ON WHIM MODEL PARAMETERS

We can use the 95% upper limits given in the previous section to constrain the physical state of the gas in filaments. In Suarez-Velázquez, Mücke & Atrio-Barandela (2013b) we described the distribution of baryons in the WHIM as a network of filaments following a log-normal distribution function. In our model baryons follow the dark matter distribution except at small scales, where baryon perturbations are damped by shock heating (Klar & Mücke 2010). At any given redshift, the cut-off scale L_{cut} is determined by the condition that the linear velocity perturbation $\mathbf{v}(\mathbf{x}, \mathbf{z})$ is equal to or larger than the sound speed $c_s = (k_B T_{\text{IGM}}(z)/m_p)^{1/2}$, with m_p the proton mass and k_B the Boltzmann constant. Then, the cut-off scale L_{cut} can be parametrized in terms of the mean Intergalactic Medium temperature, T_{IGM} . While the latter changes little with redshift (Tittley & Meiksin 2007), $L_{\text{cut}} \approx L_0(1+z)^{1/2}$. At $T_{\text{IGM}} = 10^4 \text{K}$, the cut-off scale today would be $L_0 = 1.7 h^{-1} \text{Mpc}$ (for details see Suarez-Velázquez, Mücke & Atrio-Barandela, 2013b).

To compute the tSZ effect generated by the free elec-

trons in the WHIM, we need to specify the equation of state. For shock-heated gas, the phase diagrams obtained by Kang et al. (2005) from numerical simulations can be fitted by $\log_{10}(T_e/10^8 K) = -2[\log_{10}(3.5 + x^b)]^{-1}$ with $b = \alpha + x^{-1}$ and $x = n_e/\bar{n}_B$ the electron density in units of the mean baryon density. In addition to the two parameters T_{IGM} and α , WHIM temperature anisotropies depend on σ_8 , the amplitude of the matter power spectrum on a sphere of $8h^{-1}$ Mpc, and on the fraction of free electrons in the filaments. In Figure 5 we present the radiation power spectra of the WHIM temperature anisotropies for different model parameters; we assume that all the baryons in the WHIM are ionized. In these models we fixed the Planck measured value of $\sigma_8 = 0.83$ (Planck Collaboration 2014). This corresponds to a WHIM baryon fraction of 43% to 48% for $T_{\text{IGM}} = 10^{3.6}, 10^4 K$, respectively. The spectra in panel (a) of Figure 5 represent the full contribution, obtained by integrating up to redshift $z_{\text{up}} = 3$. The contribution of filaments from earlier times is negligible. Spectra are presented in pairs, corresponding to $T_{\text{IGM}} = 10^{3.6} K$ (solid) and $10^4 K$ (dashed lines), respectively. From top to bottom, curves correspond to a equation of state parameter $\alpha = 2.0, 0.9$, respectively. In panel (b) of Figure 5 the power spectra follow the same convention. In this case the integration is restricted to $z_{\text{up}} < 0.03$, similar to the scale probed by our template.

Our formalism allows us to predict the cross-correlation of the spatial distribution of the WHIM with the tSZ distortion generated by it. As indicated in section 2.2, the matter template describes the matter distribution in the mildly non-linear regime. If the ionized gas follows the matter and its equation of state is polytropic, $T_e \propto n_e^{(\gamma-1)}$, then the pressure profile will be $P_e \propto n_e^\gamma$, where $\gamma = 1$ corresponds to isothermal gas, characteristic of the shocked regions and $\gamma = 5/3$ to adiabatic monoatomic gas. From the template $M \propto n_e$ we have constructed pressure templates with $\gamma = (1, 5/3)$. We verified that the cross-correlation at zero lag varied by less than 20% for adiabatic indices in the above range, indicating that if the template describes the distribution of the ionized WHIM, then it will also trace its tSZ contribution. Then, if a matter template, normalized to zero mean and unit variance, traces the tSZ, the cross-correlation would be $\langle TM \rangle(0) = \sigma_{\text{WHIM}}$ where $\sigma_{\text{WHIM}}^2 = \sum (2\ell + 1) C_\ell^{\text{WHIM}} / 4\pi$; therefore, the results presented in Figure 5 give the expected correlation for each set of model parameters. Additionally, we need to consider that the actual realization of the WHIM in the sky is not exactly the mean power spectrum since our template is just one realization of the sky. This gives rise to an uncertainty known as cosmic variance and given by $\epsilon_{\text{CV}} = \sum \sqrt{2(2\ell + 1) C_\ell} / 4\pi$.

In Figure 6 we present the amplitude of the cross-correlation at zero-lag, computed using the upper limit of integration $z_{\text{up}} = 0.03$, similar to the depth of our template with the upper limits obtained from the data. In panels (a) and (b) of Figure 6 the model corresponds to $T_{\text{IGM}} = 10^{3.6}, 10^4 K$, respectively. Plots follow the same convention; the thick solid blue lines represent the theoretical prediction and the surrounding shaded green area the 1σ cosmic variance uncertainty. The horizon-

tal (red) lines correspond to the 95% confidence limit given by the measured cross-correlation with the matter and the galaxy templates. The dashed (violet) line represents the correlation for an upper limit of integration $z_{\text{up}} = 0.05$ to show that by increasing the depth of our template we could probe the model very effectively. Since our error bars are dominated by the random alignments of our filaments with large scale structures in the CMB data, they will not increase significantly if our template was to trace the matter distribution out to, for example, that redshift but the signal will rise by almost a 50%. If we were not to have a detection then the constraints on model parameters would be much stronger.

Using a grid of models in the range $\sigma_8 = [0.7, 1]$, $\alpha = [1, 4]$ and $\log_{10}(T_{\text{IGM}}) = [3.4, 4.2]$ we have verified that the power spectra scales with cosmological and model parameters as $\sigma_{\text{WHIM}} \propto (\log T_{\text{IGM}})^{-1.4 \pm 0.2} \alpha^{1.7 \pm 0.2} \sigma_8^{1.3 \pm 0.1} \Omega_B$. Since σ_8 and Ω_B are fixed by observations the results of Figure 6 show that the equation of state parameter α is the most important parameter of the model. In the observationally allowed range, the variation of the model prediction with T_{IGM} is rather weak. Including cosmic variance and considering the upper limit at the 95% confidence level of the matter template, $\alpha \lesssim 1.6$ and $\lesssim 1.9$ for $T_{\text{IGM}} = 10^{3.6} K$ and $10^4 K$, respectively. The bound is much more stringent when we impose the upper limit derived from the galaxy template: $\langle TM_g \rangle(0) < 0.08 \mu K$: $\alpha \lesssim 1.1$ and $\alpha \lesssim 1.3$, respectively for the two values of T_{IGM} considered.

The upper bound in α can be translated into a constraint on the temperature of the gas at different densities using the equation of state derived from the results of Kang et al (2005). Figure 7 defines the range of the temperature of the shocked-heated WHIM as a function of its density contrast. The solid line corresponds to $\alpha = 1.0$ and the dashed lines correspond to the 95% confidence level upper limit from the matter template, $\alpha = 1.9$ (upper line) and the same limit from the galaxy template, $\alpha = 1.3$ (lower line). The shaded green area shows the region excluded by the more strict upper limit from the galaxy template that is still allowed by the matter template. For comparison we also plot the same temperature function for the numerical results of Cen & Ostriker (2006). For instance, at overdensity $x = 1$ the temperature of the electron gas is $T_e \simeq 10^{4.8} K$, while for $x = 100$ it is $T_e \lesssim 10^{7.5} K$. These temperature ranges are in agreement with the results of simulations (see Kang et al. (2005); Cen & Ostriker (2006); Bertone et al. (2010)). Still, at $T_{\text{IGM}} = 10^{3.6} - 10^4 K$ the fraction of baryons in the WHIM medium varies from 43% to 48%, providing enough room to accommodate the missing baryon fraction in the local Universe.

6. CONCLUSIONS

We have searched for the tSZ signature of the WHIM in Planck Nominal maps. To that purpose we have cleaned the frequency maps of Planck first data release from foreground emissions. These maps were correlated with a template reconstructed from the observed galaxy distribution in the 2MRS that describes the matter density field out to $\approx 90h^{-1}$ Mpc that traces the large-scale filamentary distribution of the WHIM and with a galaxy template that traces the hot circumgalactic halos. Our results showed no evidence of a WHIM-induced

tSZ temperature anisotropy to be present at any significant level or of any detectable contribution from virialized gas within low-mass halos. We set upper limits of $< 0.08 \mu\text{K}$ and $< 0.17 \mu\text{K}$ at 95% C.L. using the results from the galaxy and matter templates, respectively. We translated these upper limits into constraints on the properties of the WHIM using the model described in Suarez-Velázquez, Mückel & Atrio-Barandela (2013b). We found that the temperature of the shock-heated WHIM gas was in the range $T = 10^{4.5} - 10^{7.5} \text{K}$ at overdensities in the range $1 - 100$. The cross-correlation of the matter template and the Planck CMB data goes to zero at $\theta \sim 6^\circ$. At the median depth of our template, this angular scale would be compatible with filaments having an averaged projected size of $6 - 8 h^{-1} \text{Mpc}$. The size of filaments and the temperature of their gas is in excellent agreement with the scale and temperature range found by Van Waerbeke et al (2014), indicating that the matter template could be tracing the WHIM distribution even though it is not deep enough to produce a statistically significant signal.

The search for the missing baryons is not restricted to the CMB. Evidence of the distribution of this matter component has been obtained via UV-absorption line studies with FUSE and HST-COS (Shull et al. 2012) but these observations probe the coldest fraction of these baryons. Our results imply that most baryons would have temperatures $T \geq 10^{4.5} \text{K}$, in agreement with hydrodynamical simulations. This phase could be detected through highly ionized C, N, O, Ne, and Fe ions. In this

respect, the proposed Athena X-ray mission (Kaastra et al 2013) could provide very useful information about the WHIM parameters. With WHIM gas temperatures in the range $T = 10^{4.5} - 10^{7.5} \text{K}$, the filaments in our model can accommodate up to 48% of all the baryons. Since the tSZ effect is proportional to the electron pressure, if X-ray observations were to find that the average WHIM is larger than the limits given in Figure 7 then, to make compatible the tSZ upper limit with a higher WHIM temperature, the baryon fraction stored in filaments must decrease in a proportion similar to the temperature increment. Then, by combining observations of the WHIM at different wavelengths and different redshifts, we will measure better the physical properties of the WHIM, provide better constraints on the model parameters, improve our understanding of the physical processes undergone by the baryons during the formation of galaxies and the emergence of large scale structure, and could separate the contribution of gas in unresolved halos from that of the WHIM.

We acknowledge the use of data from the Planck/ESA mission, downloaded from the Planck Legacy Archive. RGS acknowledges financial support from the Spanish grant CONSOLIDER EPI (CSD2010-00064). FAB acknowledges financial support from the Spanish Ministerio de Educación y Ciencia (grant FIS2012-30926) and to the “Programa de Profesores Visitantes Severo Ochoa” of the Instituto de Astrofísica de Canarias. FSK is a Karl-Schwarzschild fellow at the AIP.

REFERENCES

- Anderson, M. E. & Bregman, J. N. 2011, *ApJ*, 737, 22
Atrio-Barandela, F., & Mückel, J. P. 2006, *ApJ*, 643, 1
Atrio-Barandela, F., Mückel, J. P., & Génova-Santos, R., 2008, *ApJ*, 674, L61
Bertone, S., Schaye, J., Dalla Vecchia, C., et al. 2010, *MNRAS*, 407, 544
Buote, D. A., Zappacosta, L., Fang, T., et al. 2009, *ApJ*, 695, 1351
Cen, R., & Ostriker, J.P. 1999, *ApJ*, 519, L109
Cen, R., & Ostriker, J.P. 2006, *ApJ*, 650, 560
Dai, X. Anderson, M. E., Bregman, J. N. & Miller, J.M. 2012, *ApJ*, 755, 107
Danforth, C. W., & Shull, J. M. 2008, *ApJ*, 679, 194
Davé, R., et al. 2001, *ApJ*, 552, 473
Fukugita, M., & Peebles, P.J.E. 2004, *ApJ*, 616, 643
Génova-Santos, R., Rubiño-Martín, J. A., Rebolo, R., et al. 2005, *MNRAS*, 363, 79
Génova-Santos, R., Atrio-Barandela, F., Mückel, J. P., & Klar, J.S., 2009, *ApJ*, 700, 447
Génova-Santos, R., Suarez-Velázquez, I., Atrio-Barandela, F. & Mückel, J. P. 2013, *MNRAS*, 432, 2480
Gorski, K. et al 2005, *ApJ*, 622, 759
Hernández-Monteagudo, C., Génova-Santos, R., & Atrio-Barandela, F., 2004, *ApJ*, 613, L89
Heß, S., Kitaura, F.-S., & Gottlöber, S. 2013, *MNRAS*, 435, 2065
Huchra, J. P., Macri, L. M., Masters, K. L., et al. 2012, *ApJS*, 199, 26
Kaastra, J., Finoguenov, A., Nicastro, F. et al. 2013, *arXiv:1306.2324*
Kang, H., Ryu, D., Cen, R., & Song, D. 2005, *ApJ*, 620, 21
Kitaura, F.-S. (2012a) *MNRAS*, 420, 2737
Kitaura, F.-S., Erdogdu, P., Nuza, S. E., Khalatyan, A., Angulo, R. E., Hoffman, Y., Gottlöber, S., 2012b, *MNRAS*, 427, 35
Klar, J. S., & Mückel, J. P. 2010, *A&A*, 522, 114
Molnar, S. M., & Birkinshaw, M. 1998, *ApJ*, 497, 1
Nicastro, F., Mathur, S., Elvis, M., et al. 2005, *ApJ*, 629, 700
Planck Collaboration. Planck Intermediate Results VIII, 2013a, *A&A*, 550, 134
Planck Collaboration. Planck Intermediate Results XI, 2013b, *A&A*, 557, 52
Planck Collaboration. Planck explanatory supplement. First release v1.00 2013
http://wiki.cosmos.esa.int/planckpla/index.php/Main_Page
Planck Collaboration. Planck 2013 Results I, 2014a, *A&A*, 571, 1
Planck Collaboration. Planck 2013 Results VI, 2014b, *A&A*, 571, 6
Planck Collaboration. Planck 2013 Results XI, 2014c, *A&A*, 571, 11
Planck Collaboration. Planck 2013 Results XII, 2014d, *A&A*, 571, 12
Planck Collaboration. Planck 2013 Results XIII, 2014e, *A&A*, 571, 13
Planck Collaboration. Planck 2013 Results XVI, 2014f, *A&A*, 571, 16
Planck Collaboration. Planck 2013 Results XXI, 2014g, *A&A*, 571, 21
Rauch, M., Miralda-Escudé, J. & Sargent, W. L. 1997, *ApJ*, 489, 7
Suarez-Velázquez, I., Kitaura, F.-S., Atrio-Barandela, F. & Mückel, J. P., 2013a, *ApJ*, 769, 25
Suarez-Velázquez, I. F., Mückel, J. P., & Atrio-Barandela, F. 2013b, *MNRAS*, 431, 342
Shull, J. M., Smith, B. D., & Danforth, D. W. 2012, *ApJ*, 759, 23
Sunyaev, R. A., & Zel’dovich, Y. B. 1970, *ApSS*, 7, 3
Tittley E., Meiksin A., 2007, *MNRAS*, 380, 1369
Tripp, T. M., Sembach, K. R., Bowen, D. V., et al. 2008, *ApJS*, 177, 39
Ursino, E., Galeazzi, M. & Haffenberger, K. 2014, *ApJ*, 789, 55
Van Waerbeke, L., Hinshaw, G. & Murray, N. 2014, *PRD*, 89, 023508

Werner, N., Finoguenov, A., Kaastra, J. S., et al. 2008, A&A, 482, L29
Weinberg, D. H., Miralda-Escudé, J., Hernquist, L. & Katz, N. 1997, ApJ, 490, 564
Williams, R. J., Mulchaey, J. S., & Kollmeier, J. A. 2013, ApJ, 762, LL10

Yao, Y., Shull, J. M., Wang, Q. D. & Cash, W. 2012, ApJ, 746, 166

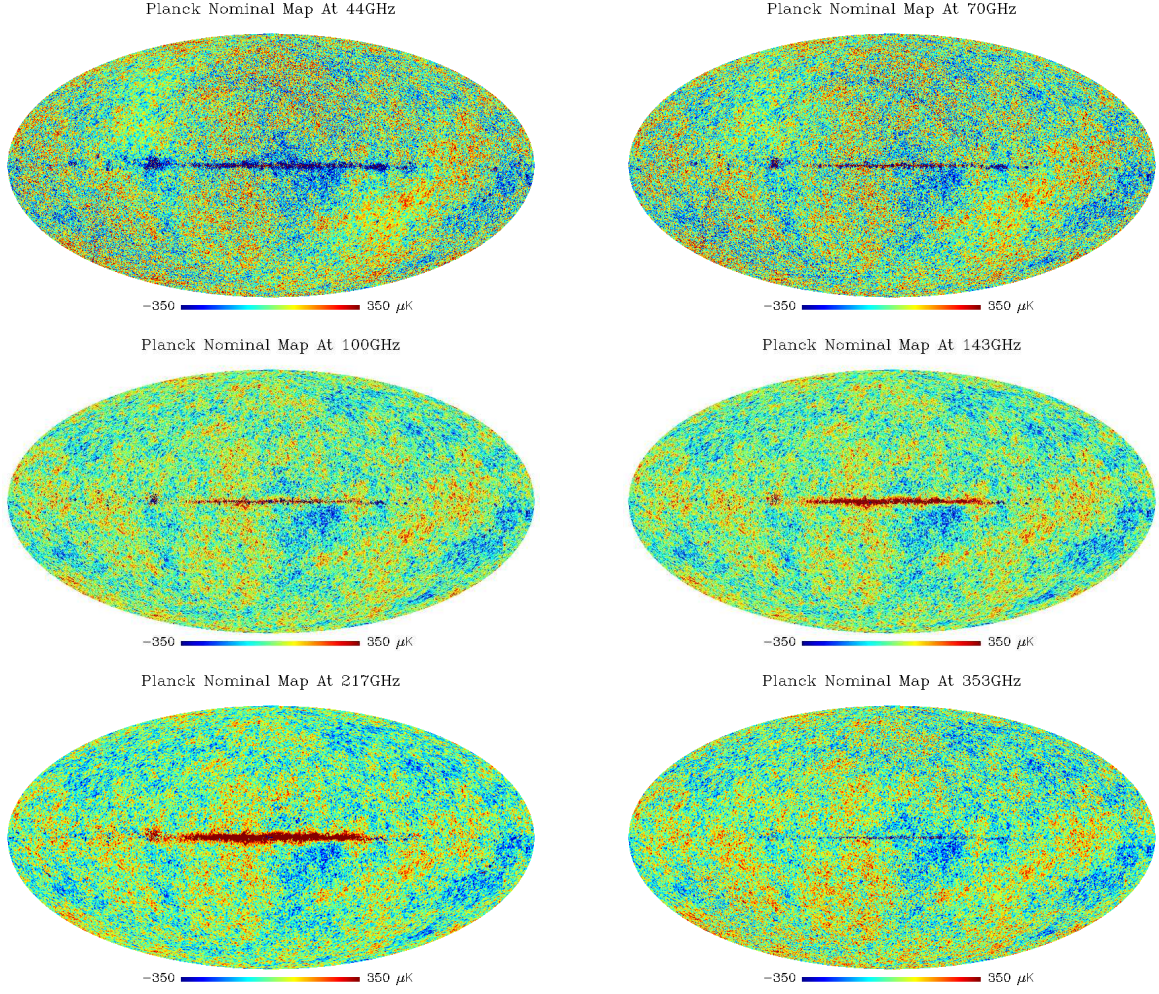


FIG. 1.— Foreground cleaned Planck Nominal maps at different frequencies. From top to bottom and left to right, frequencies are 44, 70, 100, 143, 217 and 353 GHz. A detailed explanation of the cleaning methodology is given in section 2.1. Apart from some small foreground residuals along the Galactic plane (which are positive in the case of the thermal dust emission and negative for the synchrotron emission), these maps are dominated by primordial CMB.

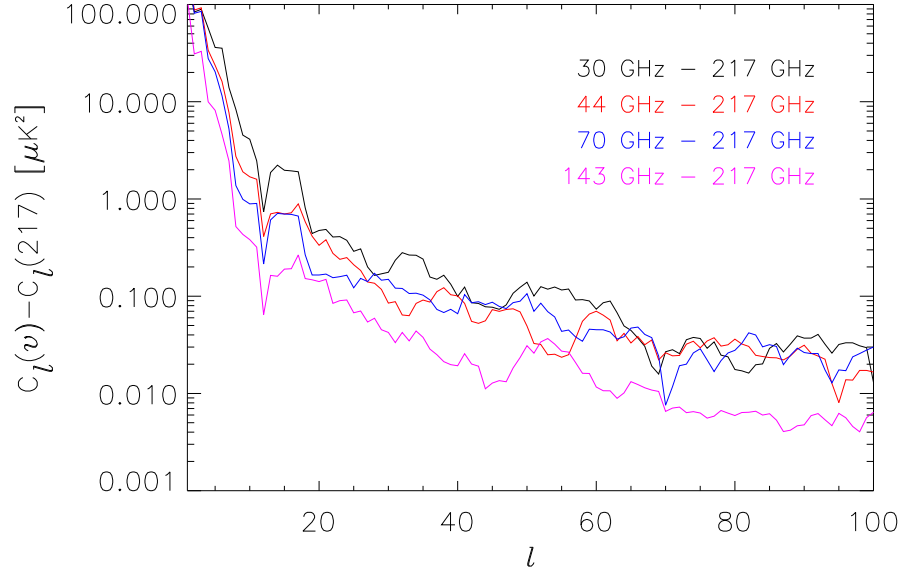


FIG. 2.— Power spectra of the foreground cleaned Planck Nominal maps, after dividing by the window function of each frequency and subtracting the 217 GHz channel. The increase in power at low multipoles could be produced by a combination of detector $1/f$ correlated noise and foreground residuals. To remove this effect we filter the cleaned maps by removing all multipoles with $\ell < 20$, as explained in section 3.

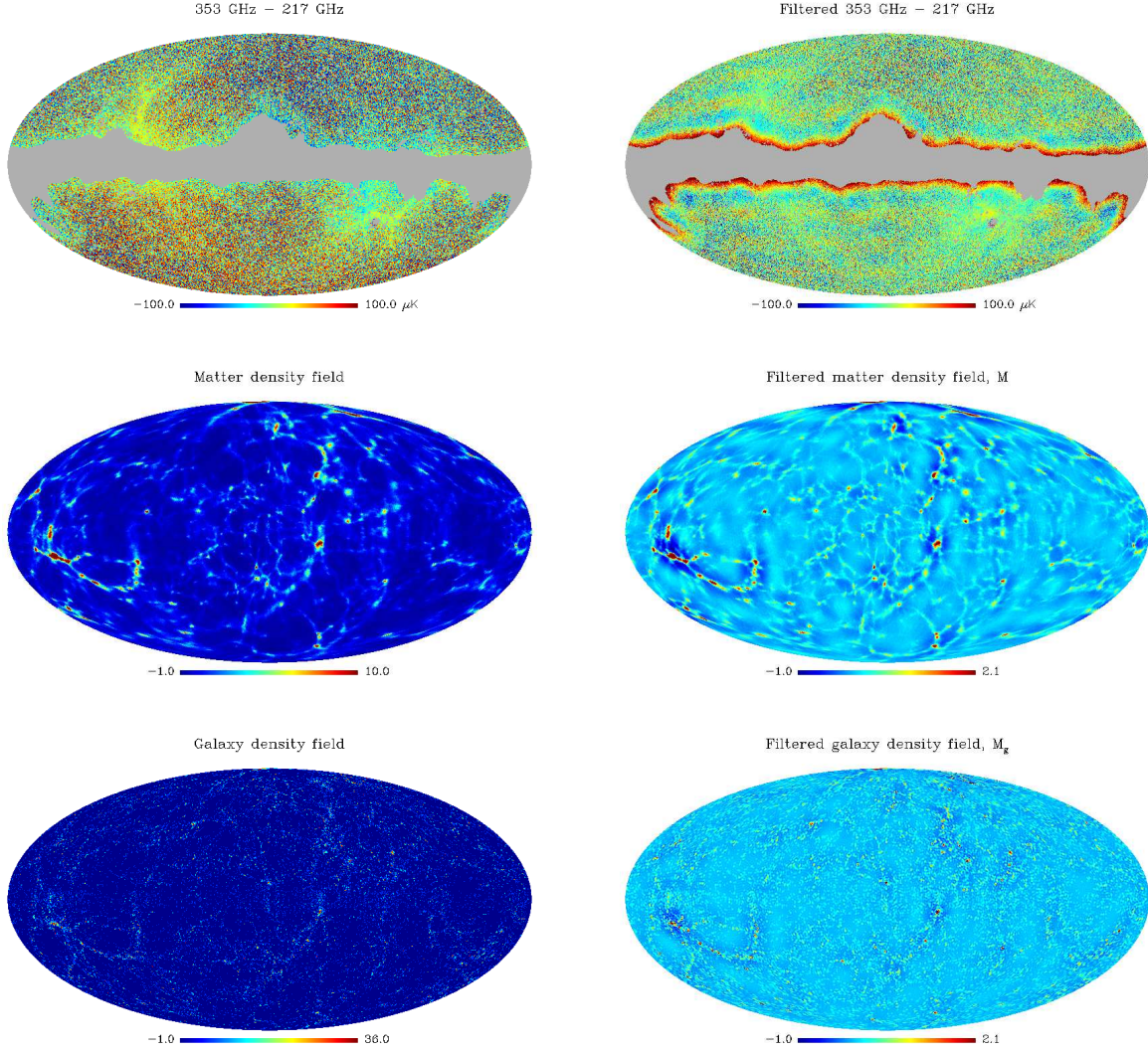


FIG. 3.— Comparison of the original CMB data and templates with their filtered counterparts obtained by removing all multipoles with $\ell < 20$. Top row: original Planck Nominal map at 353 GHz minus 217 GHz (left) and filtered map (right). The mask applied to the data removes 20% of the sky. Middle row: original (left) and filtered (right) matter template. Bottom row: original template of projected density of galaxies (left) and filtered (right) template.

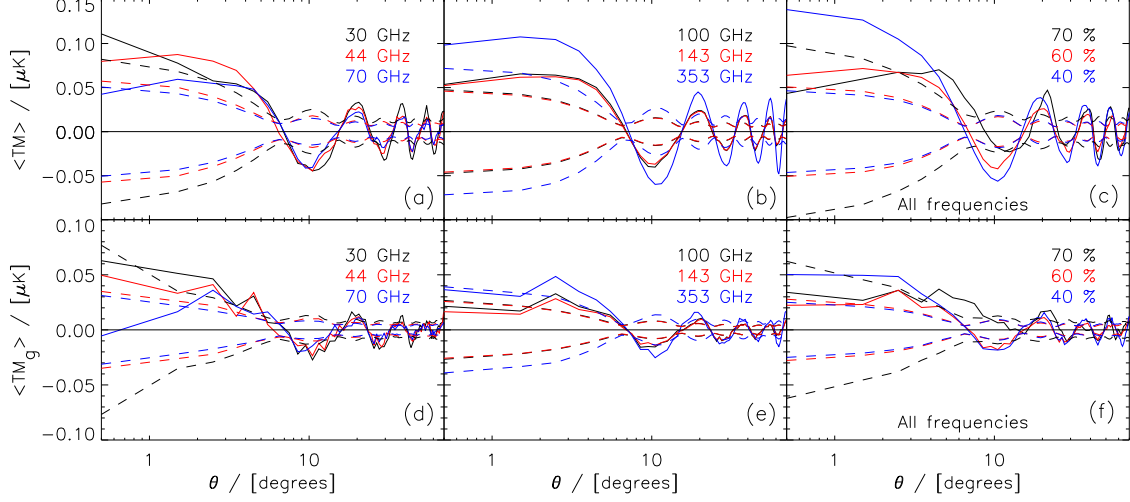


FIG. 4.— Cross-correlation of filtered matter (top row) and galaxy density (bottom row) templates with the foreground cleaned Planck Nominal maps divided by the frequency dependence of the tSZ effect; at the different frequencies the cosmological signal was removed by subtracting the 217 GHz channel. Solid lines represent the data and dashed lines the error bars. In (a,b) and (d,e) we plot the correlations with the LFI and the HFI channels, respectively, calculated using the mask that retains 60% of the sky. In (c,f) we plot the average correlation of all frequencies obtained after masking different fractions of the sky. The percentage indicates the fraction of the sky used.

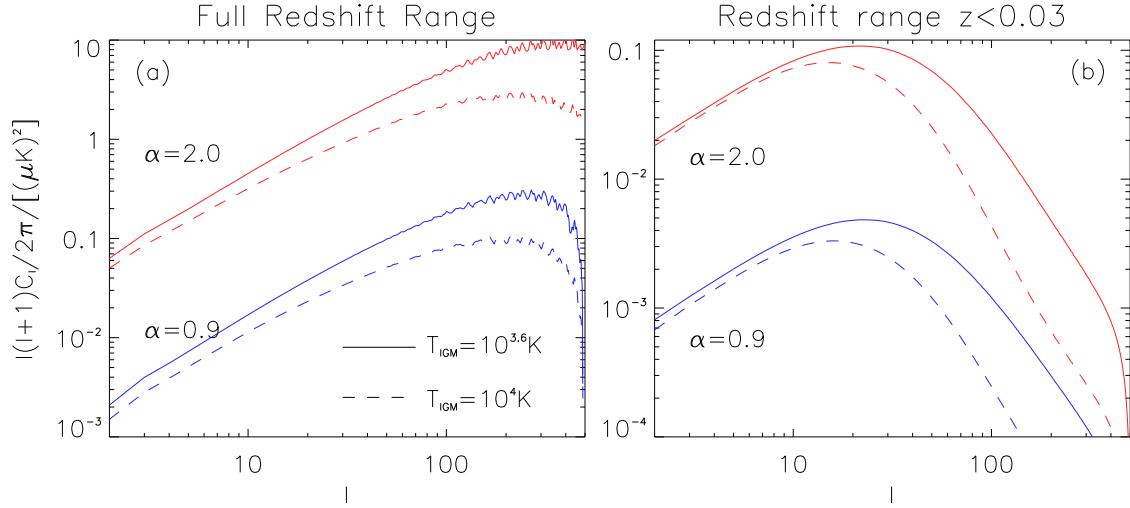


FIG. 5.— Power spectra of the tSZ due to the WHIM for different model parameters. As indicated the spectra in panel (a) includes the contribution at all redshifts, while the spectra in panel (b) only includes the contribution up to $z_{\text{up}} = 0.03$. Solid and dashed lines correspond to $T_{\text{IGM}} = 10^{3.6}$ K and 10^4 K, respectively; neighboring graphs, given in the same color, correspond to the same value of the equation of state parameter α , in decreasing amplitude from top to bottom.

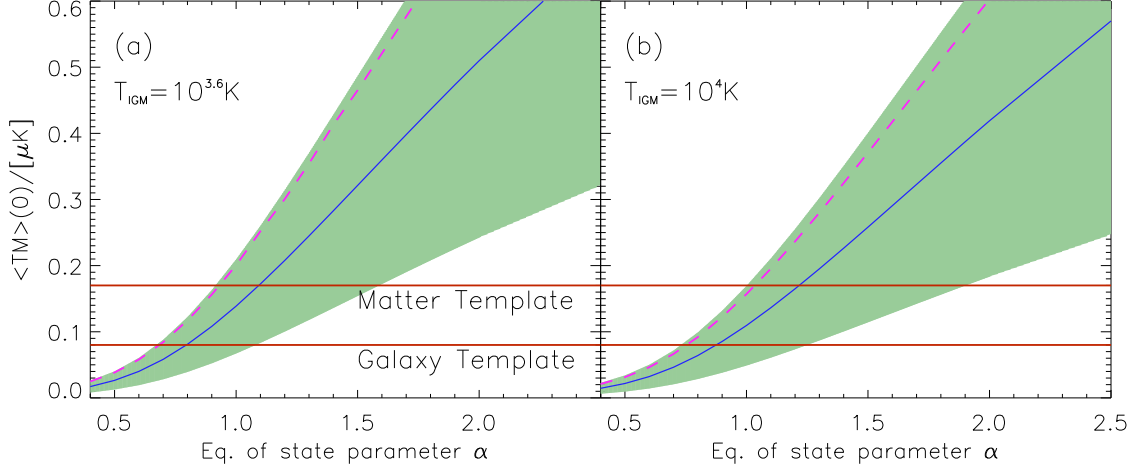


FIG. 6.— Comparison of the measured and the predicted amplitude of the cross-correlation of the matter template that traces the matter distribution out to $z_{\text{up}} = 0.03$ and the tSZ anisotropy due to the WHIM. The horizontal red lines give the upper limit of the measured correlation at zero lag at the 95% confidence levels derived from the matter template and the galaxy templates. The blue solid line and the shaded green area represent the expected cross-correlation and the 1σ cosmic variance uncertainty for different model parameters, considering a maximum redshift $z_{\text{up}} = 0.03$ for the matter density field traced by the template. The dashed violet line represents the predicted cross-correlation for $z_{\text{up}} = 0.05$. In panel (a) and (b) the IGM temperature is $T_{\text{IGM}} = 10^{3.6}\text{K}$ and 10^4K , respectively.

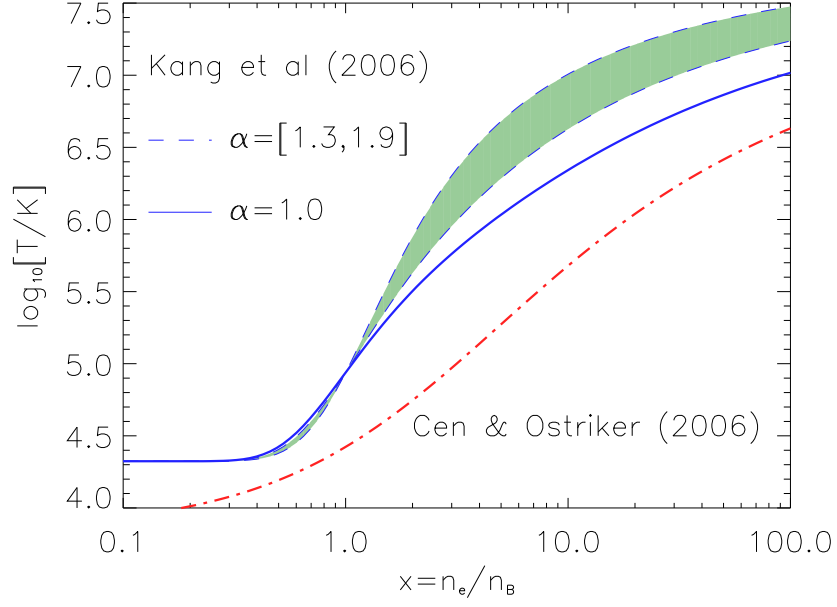


FIG. 7.— The blue solid line represents the temperature of the shock-heated WHIM for different overdensities in the Kang et al (2005) numerical fit for an equation of state parameter $\alpha = 1$. The blue dashed lines correspond to $\alpha = 1.3$ (bottom) and $\alpha = 1.9$ (top), the 95% upper limits from the galaxy and matter templates, respectively. The shaded green area shows the region excluded by the more strict constraint of the galaxy template that is allowed by the matter template. For comparison, the dot-dashed red line represents the temperature-overdensity relation from Cen & Ostriker (2006).